Drag Force in Discrete Particle Models—Continuum Scale or Single Particle Scale?

S. H. L. Kriebitzsch, M. A. van der Hoef, and J. A. M. Kuipers
Dept. of Chemical Engineering and Chemistry, Eindhoven University of Technology, 5600 MB Eindhoven, The Netherlands

DOI 10.1002/aic.13804
Published online April 23, 2012 in Wiley Online Library (wileyonlinelibrary.com).

Unresolved discrete particle (DP) models, where a Lagrangian method is used for the solid phase, and a Eulerian method for the fluid phase, have become increasingly popular. The fluctuations of the drag force on individual particles in a homogeneous random array obtained from fully resolved simulations using a lattice Boltzmann method were analysed; such fluctuations are by construction ignored in the unresolved DP model. The drag on individual particles in the array can differ up to 40% with the drag that would be used in DP type simulations was found. A detailed analysis shows that the drag on an individual particle depends strongly on all its surrounding neighbors within a distance of at least two particle diameters. As in DP models, the local flow field is unresolved, the conclusion is that this root mean square (RMS) deviation in the drag force is inherent to the model. © 2012 American Institute of Chemical Engineers *AIChE J,* 59: 316–324, 2013
Keywords: particulate flows, drag force, computational fluid dynamics, multiscale modeling

Introduction

Gas-solid flows appear in many processes within the process industries. A widely used type of process equipment for efficient gas-solid contacting are fluidized beds. Although the fluidized bed technology was established about 80 years ago, quantitative predictions of their behavior using numerical calculations still remains a challenge due to very different time and length scales present in fluidized beds. Fully resolved simulation of large industrial equipment is not feasible due to the limited computational power available and time constraints typically imposed on projects conducted in industry. Consequently, continuum models, such as two-fluid models (TFM), are used to predict the macroscopic flow patterns. These models can be obtained by averaging the equations of motion of both the particle and the fluid phase.[1,2] As the details of the flow on the scale of a few particle diameters are averaged out, closures are needed to account for particle–particle interaction and gas–particle interaction.[3] These closures can be obtained from theory, experiment, or simulations of smaller systems which allow to resolve smaller length scales of the flow problem at hand.[4]

In recent years, discrete particle models (DPM), also called discrete element models (DEM), have become increasingly popular. In these models, the continuum description for the solid phase is replaced by a discrete representation, where the Newtonian equations of motion for each particle are solved. Collisions between individual particles are explicitly computed, implying that discrete particle (DP) models allows for a much more accurate description of the particle–particle interactions. Ideally, one would like a similar situation for the gas–particle interactions, where the flow between the particles is fully resolved, and the interaction is modeled at the level of the particle's surface (for instance by no-slip boundary conditions). However, even for small system sizes (20,000 particles), such simulations are prohibitively expensive due to the large number of grid points that are required in computational fluid dynamics (CFD). For this reason, in DEM models, an averaged equation of motion is solved for the gas phase just like in the TFM where closures for the gas-solid interaction force $\vec{F}_{g\rightarrow i}$ are required.

Closures currently available were obtained for systems considered to be homogeneous and only the mean drag is characterized as a function of the average porosity and slip velocity. In other words, these drag closures readily fit into two-fluid modeling of fluidized beds, at least in homogeneous regions of a fluidized bed. In DP models, however, the equation of motion for each particle is solved, and thus, the forces acting on each individual particle must be computed. This force depends however on the local flow field around the particle, thus on information that is not available. Therefore, usually the same closures as in TFM are used and porosity and slip velocity are obtained by interpolating Eulerian quantities (flow velocity $\vec{u}$ and porosity ε) to the position of the particle. If one is consistent with the way the drag correlations are derived, one should use the cell-average slip velocity $\vec{u}-\vec{v}$ to compute the drag force ($\vec{v}$ being the cell-average solid velocity); however, in DP models, it is common practice to use the individual slip velocity $\vec{u}-\vec{v}_i$, so that each particle feels a different drag force, which would seem more realistic than a uniform drag force. However, even for static systems, the true drag force on each particle will not be uniform across the cell, due to variations in the local microstructure, in other words, due to local

Correspondence concerning this article should be addressed to S. H. L. Kriebitzsch at S.H.L.Kriebitzsch@tue.nl.

heterogeneities. The goal of this article is to investigate in detail how large these variations are. To this end, results obtained from direct numerical simulation (DNS) simulations at low-Reynolds number flow in static, random arrays of spheres are presented. The drag acting on individual particles obtained from these simulations will be compared to the drag that one would calculate for these particles in a DP model simulation. Not we do not perform a DPM simulation, rather we compute a gas-solid force for each particles as if it were in a DPM simulation.

As we will show, it turns out that even for systems where the distribution of the solid phase would be considered as homogeneous, that the fluctuations can be substantial—which means that the drag force as calculated in the current class of DP models with a cell-average porosity, can be quite different from the true drag force, even when the most accurate and suitable drag correlations are used. This raises the question if any improvement can be made using information on the local microstructure of a particle, which is available because in a DP model simulation, all particle positions are known. In particular, we investigate the concept of using an individual porosity (via a Voronoi tessellation) to improve the estimate of the drag force on particles, just like one uses the individual particle velocity instead of the cell-average. Interestingly, it turns out that the disagreement with the DNS results even gets worse. The reason is that variations in the local structure will lead to variations in the local flow field, which cannot be accounted for in a DEM framework. This flow field is influenced not only by the nearest neighbors but also by distant particles. The final conclusion is that the drag force as calculated in DEM simulations of homogeneous gas-solid systems, deviates on average 10% from the true drag force, and that there is no simple solution to improve on this. The precise effect of these deviations on larger-scale phenomena such as the onset of bubbling in fluidized beds remains to be investigated.

Models and Method

Fluid-particle force in DP models

In this article we will compare the fluid-particle force as obtained from DNS to a fluid-particle force that would follow from DPM-type drag closures. Therefore, we shortly introduce the DP model and its basic equations. Averaged equations of continuity and motion are used to describe the fluid phase

$$\frac{\partial}{\partial t}\varepsilon\rho_f = \vec{\nabla}\cdot\left(\varepsilon\rho_f\vec{u}\right) \tag{1}$$

$$\frac{\partial}{\partial t}\left(\varepsilon\rho_f\vec{u}\right) + \vec{\nabla}\cdot\left(\varepsilon\rho_f\vec{u}\vec{u}\right) = -\vec{\nabla}p - \vec{\nabla}\cdot(\varepsilon\tau) + \varepsilon\rho_f\vec{g} - \vec{f}_{f,s} \tag{2}$$

with $\vec{u}$ being the fluid velocity, ρ_f is the density, p is the pressure, τ is the viscous stress tensor, $\vec{g}$ is the gravity, and ε is the porosity and $\vec{f}_{f,s}$ is the force density arising from the interaction with the solid particles (to be discussed later). Equations (1) and (2) are usually solved on a computational grid with a grid size h of a few particle diameters as illustrated in Figure 1. The particles are usually modeled as spheres and Newtons equation of motion is solved for each particle i

$$V_i\rho_{p,i}\frac{d}{dt}\vec{v}_i = V_i\rho_{p,i}\vec{g} + \vec{F}_{c,i} + \vec{F}_{f,i} \tag{3}$$

where ρ_i and V_i are the density and volume of particle i, and $\vec{F}_{c,i}$ is the collision force due to contact with other solid objects.

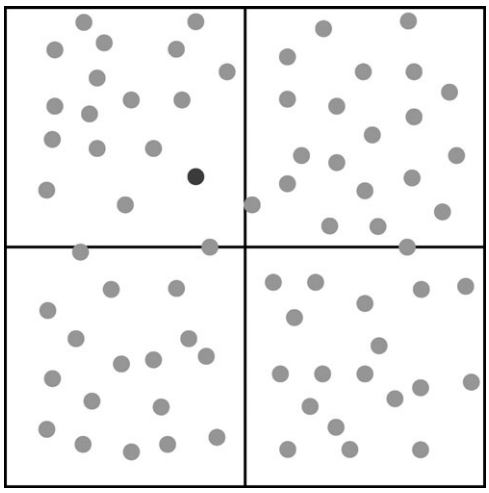

Figure 1. Computational grid used in DPM simulations.

Both equations are coupled by the porosity $\varepsilon(\vec{x})$, the fluid-particle force $\vec{F}_{f,i}$, and the fluid-solid force density $\vec{f}_{f,s}$. The porosity entering Eq. 2 is readily calculated from the known particle positions $\vec{r}_i$ and particle volumes $V_{p,i}$ by averaging over a length l_c which is typically comparable to the grid size h used to solve the partial differential equations (2)

$$\varepsilon(\vec{x}) = \frac{\sum_i D\left(\vec{x}-\overrightarrow{r_i}\right)V_{p,i}(\overrightarrow{r_i})}{l_c^3} \tag{4}$$

$D\left(\vec{x}-\overrightarrow{r_i}\right)$ is a Eulerian–Lagrangian mapping function (see e.g., Kitagawa et al.[5]), that has a finite support $(D\left(\vec{x}-\overrightarrow{r_i}\right)=0,\ \text{if}\ \left|\vec{x}-\overrightarrow{r_i}\right| \geq l_c)$.

If the fluid-particle force $\vec{F}_{f,i}$ is known, then, the Eulerian force density $\vec{f}_{f,s}$ can in principle be obtained by a similar procedure

$$\vec{f}_{f,s}(\vec{x}) = -\frac{\sum_i D(\vec{x}-\overrightarrow{r_i})\vec{F}_{f,i}}{l_c^3} \tag{5}$$

As mentioned earlier, the drag force exerted on an individual particle is calculated using closures which were obtained in the framework of continuum description of the solids phase. Therefore, the drag is typically calculated from equations like

$$\vec{F}_{f,i} = F(\bar{\varepsilon}_i, \overline{Re}_i)\cdot 3\pi\mu_f d_p(\bar{\vec{u}}_i - \bar{\vec{v}}_i) \tag{6}$$

that is, a dimensionless coefficient F times the Stokes drag, which is estimated from a drag correlation. The overbar and subscript i indicate that this quantity is first calculated on the Eulerian grid and then interpolated to the Lagrangian particle position $\vec{x}_i$. Typically, tri-linear interpolation is used to calculate the porosity$\bar{\varepsilon}_i$, the fluid velocity $\bar{\vec{u}}_i$, and the mean solid velocity $\bar{\vec{v}}_i$ (see e.g., Ouyang and Li,[6] Helland et. al.,[7] van Wachem et. al.,[8] Kafui et. al.[9]). The Reynolds number $\overline{Re}_i$ is then calculated from these interpolated quantities. Note that in most DP model codes, the individual particle velocity $\vec{v}_i$ is used instead of $\bar{\vec{v}}_i$, as an *ad hoc* modification.[6–9]

As we are only considering low-Reynolds number flows in this work, we will use a correlation for the dimensionless drag force F recently derived by van der Hoef et al.[10]

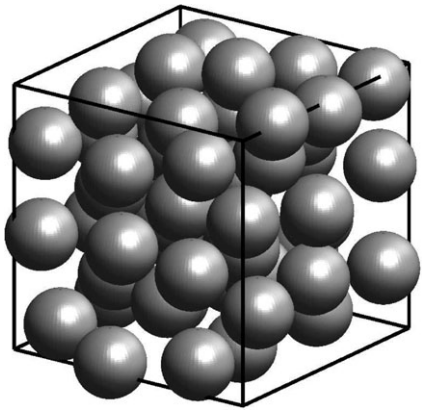

Figure 2. Example of an configuration with 54 particles used in the simulations.

$$F(\varepsilon,0)=\frac{10(1-\varepsilon)}{\varepsilon^3}+\varepsilon\left(1+1.5\sqrt{1-\varepsilon}\right) \tag{7}$$

Note that in this work, we consider the total gas-solid interaction force and not the drag force, which differ by a factor of ε for monodisperse systems (see van der Hoef et al.[10]).

Simulation method

The flow field was solved using the SUSP3D lattice Boltzmann code, which is described in detail by Ladd[11] and some recent updates by Verberg and Ladd.[12] The computational domain was fully periodic and a simple bounce-back rule was applied to enforce no-slip on the particle surface. The random arrays of spheres were obtained by a standard Monte–Carlo procedure. First, they were placed in an ordered cubic structure and then a Monte–Carlo algorithm for hard-spheres was applied. A typical result of this procedure is shown in Figure 2.

All particles move with the same velocity v and a uniform force is applied to the gas phase to ensure a zero-net momentum flux into the system. By that the mean superficial velocity in a frame of reference moving with the particles is

$$\vec{U}=\varepsilon\cdot(\vec{u}-\vec{v})=-\vec{v} \tag{8}$$

For the results presented, typically 10–20 independent simulations with 54 particles were done for each porosity such that the total particle number N_p was between 540 and 1080. The direction of the velocity was chosen randomly in these simulations. More details can be found in van der Hoef et al.[10] The result for the total gas-solid interaction force acting on each particle as obtained from the DNS calculation will be compared with the force that would be computed in a DP model simulation, from Eq. 6. In that case, the total domain (for example, see Figure 2) is in fact represented as a single CFD cell. The slip velocity $\bar{\vec{u}}_i-\vec{v}_i$ is then equal to $-\vec{v}/\varepsilon$ for each particle, so that

$$\vec{F}_{f,i}=-F(\bar{\varepsilon}_i,0)\cdot 3\pi\mu_f d_p\vec{v}$$

where we assumed that the Reynolds number could be set to zero. In a standard DP model simulation, the porosity $\bar{\varepsilon}_i$ is calculated from an interpolation of the nearest computational CFD cells. In this case, these would be periodic images, and for each particle, the value ε would be obtained, so

$$\vec{F}_f^{\,\mathrm{I}}=-F(\varepsilon,0)\cdot 3\pi\mu_f d_p\vec{v} \tag{9}$$

that is, the same for each particle in the domain (so, we dropped the subscript i). We will also compare the result if the true, local porosity ε_i of each particle i would be used (see next section)

$$\vec{F}_{f,i}^{\,\mathrm{II}}=-F(\varepsilon_i,0)\cdot 3\pi\mu_f d_p\vec{v} \tag{10}$$

which will yield a different force on each particle due to the variation in the local porosity. To distinguish between the two "DP model"-fluid–particle forces, a superscript I and II has been added.

Local porosity and Voronoi tessellation

In DP models, information on the microstructure of the particle ensemble is explicitly available because the position of all particles is known. Therefore introduce a local porosity ε_i for each particle i based on the concept of Voronoi tessellation. The Voronoi tessellation divides the computational domain in a set of volumes V_i^{vor}, such that each point within the volume is closer to surface of the particle i than to any neighboring particle $j\neq i$. In this way, a unique decomposition of space is obtained, a 2D example of which is shown in Figure 3. For monodisperse systems, one obtains a set of polyhedra but in the more general case of polydisperse particle system one has volumes with curved edges and surfaces.[13]

The difference of the Voronoi volume V_i^{vor} and the volume V_i of particle i can be considered as the "free" volume that each particle feels and we define the local porosity ε_i for each particle as

$$\varepsilon_i=\frac{V_i^{\mathrm{vor}}-V_i}{V_i^{\mathrm{vor}}} \tag{11}$$

Results

The drag on individual particles and deviations from correlations

In this section, we quantify the deviation of the "true" fluid-particle force on an individual particle (as obtained from DNS simulations) from the force that one would predict in DP model simulations. To this end, we have to make

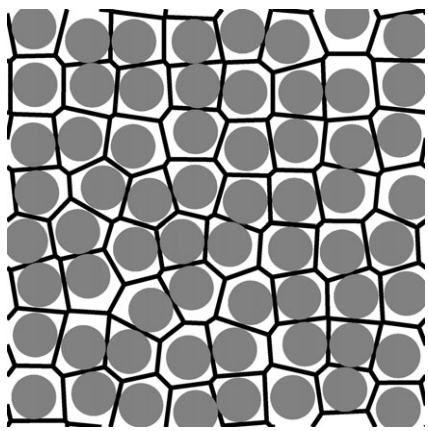

Figure 3. Voronoi diagram in 2-D periodic array of monodisperse spheres.

two modifications to the raw DNS data to make a clean comparison:

1. By definition $\vec{F}_{f,i}$ is in the direction of flow, however, the direction of the fluid–particle force $\vec{F}_i^{\mathrm{LB}}$ as calculated by the lattice Boltzmann method may deviate from $\vec{U}$. We, therefore, compare $\vec{F}_f^{\mathrm{I}}$ and $\vec{F}_{f,i}^{\mathrm{II}}$ with the component of $\vec{F}_i^{\mathrm{LB}}$ in the direction of flow, defined by

$$\vec{F}_{f,i}^{\mathrm{LB}} = \frac{\left(\vec{F}_i^{\mathrm{LB}} \cdot \vec{U}\right)\vec{U}}{\vec{U} \cdot \vec{U}} \tag{12}$$

As $\vec{F}_f^{\mathrm{I}}$, $\vec{F}_{f,i}^{\mathrm{II}}$, and $\vec{F}_{f,i}^{LB}$ are now all in the same direction, we can just compare the absolute values F_f^{I}, $F_{f,i}^{\mathrm{II}}$, and $F_{f,i}^{\mathrm{LB}}$.

2. Our goal is to show the fluctuations and not systematic deviations between DNS results and drag force correlations, hence, we enforce the average DNS drag force in the computational domain to be equal to the drag calculated from Eqs. 9 and 7 using the average porosity and slip velocity, by adding (or subtracting) a small amount to each $F_{f,i}^{\mathrm{LB}}$ so that it satisfies

$$\langle F_f^{\mathrm{LB}} \rangle = \frac{1}{N_p} \sum_{i=1}^{N} F_{f,i}^{\mathrm{LB}} = F_f^{\mathrm{I}}$$

Note that Eq. 7 was obtained from similar type of computational data, and therefore, this correction was in all cases of O(1%) or smaller.

In Figure 4, we show the distribution of the relative difference

$$\Delta F_i^{\mathrm{LB,I}} = \frac{F_{f,i}^{\mathrm{LB}} - F_f^{\mathrm{I}}}{\langle F_f^{\mathrm{LB}} \rangle} \tag{13}$$

of the drag obtained from DNS with the drag calculated using Eqs. 9 and 7 for different mean porosities is shown. As by construction, the predicted drag F_f^{I} is equal to the mean of $F_{f,i}^{\mathrm{LB}}$, this figure can also be regarded as the fluctuation of the actual drag $F_{f,i}^{\mathrm{LB}}$ for each particle with respect to the mean drag $\langle F_f^{\mathrm{LB}} \rangle$. One sees that the actual drag acting on individual particles differs up to about 40% from the predicted drag using average values for porosity and slip-velocity.

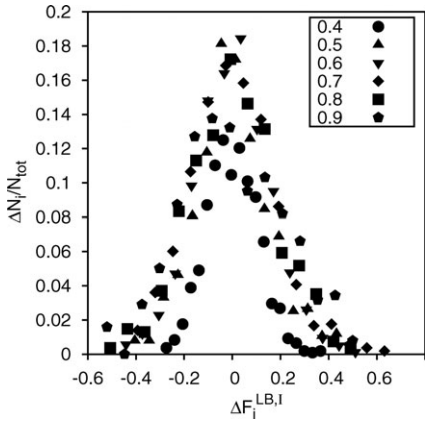

Figure 4. Distribution of the deviation $\Delta F_i^{\mathrm{LB,I}} = \frac{F_{f,i}^{\mathrm{LB}} - F_{f,i}^{\mathrm{I}}}{\langle F_f^{\mathrm{LB}} \rangle}$ of the drag force on individual particles from the mean for different porosities.

Note that the error in the force on individual particles due to grid resolution and other numerical parameters is typically about 3% or less.

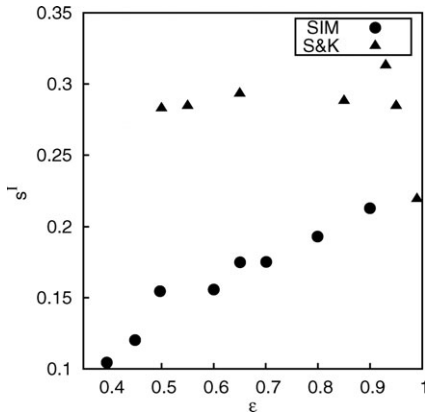

Figure 5. Mean relative deviation s^{I} (14) of the drag force on an individual particle and the average drag as a function of the mean porosity.

For comparison, we also included data for the variance of the gas-solid force given by Koch and Sangani.[14]

Figure 5 shows the mean relative deviation s^{I}

$$s^{\mathrm{I}} = \sqrt{\frac{\sum_{i=1}^{N_{\mathrm{P}}} (\Delta F_i^{\mathrm{LB,I}})^2}{N_{\mathrm{P}} - 1}} \tag{14}$$

normalized by the mean drag as a function of the porosity. For a low porosity of $\varepsilon \approx 0.4$, the mean deviation is about 10% and increases to about 20% for a porosity of $\varepsilon \approx 0.9$. In other words, even for these systems which are considered homogeneous and in the creeping flow regime, the drag forces on individual particles predicted in DP model simulations will differ on average at least 10% from the true drag force. We also included the data for the variance in the gas-solid force from Stokesian dynamics simulation by Sangani and Koch. We see significant deviations between the two results, although the Sangani and Koch datapoint for $\varepsilon = 0.99$ seems consistent with our data. At present, we have no explanation for the deviation. We have checked that the discrepancy was not caused by the fact that we use a small, but finite Reynolds number (0.2). Simulations using $Re = 2.1$ gave no different results (see also Fig. 13). The effect of the grid size was negligible: using $d_p/h = 6.7$, 8.7, and 12.7 did not have an significant effect on the fluctuations.

In general, the "true" force $\vec{F}_i^{\mathrm{LB}}$ as measured in a DNS simulation will not be exactly in the direction of the relative superficial velocity $\vec{U}$, but inclined by some angle

$$\alpha = \angle\left(\vec{F}_i^{\mathrm{LB}}, \vec{U}\right) \tag{15}$$

with the relative superficial velocity $\vec{U}$ and, thus, with the drag force $\vec{F}_f^{\mathrm{I}}$. Note that we computed the angle between the two vectors $\vec{U}$ and $\vec{F}^{\mathrm{LB}}$ from

$$\cos\alpha = \frac{\vec{F}^{\mathrm{LB}} \cdot \vec{U}}{\left|\vec{U}\right|\left|\vec{F}^{\mathrm{LB}}\right|}$$

Hence, there is no sign associated with α and we obtain the distribution of this angle as shown in Figure 6. Surprisingly, for all porosities, a similar distribution is found. The mode is at about 6° and the maximum about 20°. For most particles, the gas-solid interaction force is only slightly

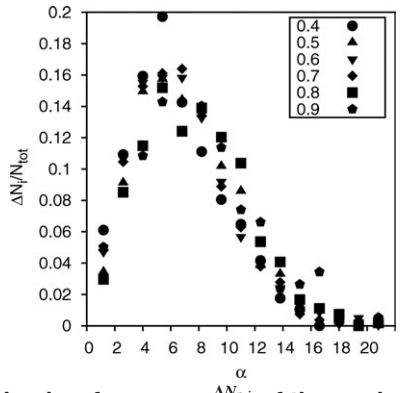

Figure 6. Number frequency $\frac{\Delta N_{p,i}}{N_p}$ of the angle α between the measured force $\vec{F}_i^{LB}$ and the superficial velocity U.

inclined with respect to the mean flow direction. The difference in the absolute value of drag and total force can be calculated from

$$\frac{\left|\left|\vec{F}_i^{LB}\right| - \left|\vec{F}_{f,i}^{LB}\right|\right|}{\left|\vec{F}_i^{LB}\right|} = \left|\left(1 - \frac{\left|\vec{F}_{f,i}^{LB}\right|}{\left|\vec{F}_i^{LB}\right|}\right)\right| = (1 - \cos(\alpha)) \qquad (16)$$

Using the values for α as shown in Figure 6, one sees that on average the projected force $F_{D,i}^{LB}$ differs by less than O(1%) or less from the true force F_i^{LB} and the maximum difference is 10%. Hence, the fluctuations of the drag on individual particles $\vec{F}_{f,i}^{LB}$ with respect to the mean are larger than difference between $\vec{F}_{f,i}^{LB}$ and $\vec{F}_i^{LB}$. Thus, it is the magnitude of the gas-solid interaction which differs from particle to particle and the fluctuations do not stem from the projection of the gas-solid interaction force onto the direction of the mean flow $\vec{U}$.

Prediction of the drag force using a Voronoi tessellation-based local porosity

In DP model simulations, information on the local microstructure of all particles is known due to the Lagrangian description of the particles, and local quantities, such as a local porosity ε_i (see Ref. 11), can be calculated for each individual particle. The distribution of the local porosity with respect to the mean porosity for the systems studied is shown Figure 7. For all mean porosities the local porosities,

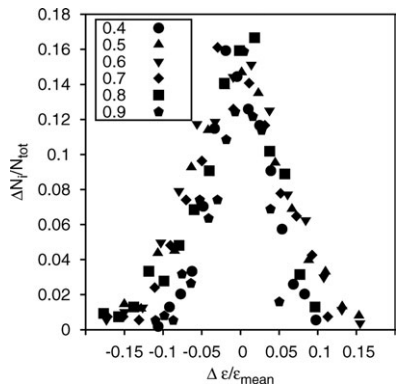

Figure 7. Distribution of the local porosities ε_i for different mean porosities ε.

are evenly distributed around the mean with a maximum deviation up to 15%. As also the drag is evenly distributed around its mean (Figure 5), one might be tempted to use a local porosity to improve agreement of DNS results and DP model representation of the drag. If we assume that ε_i suffices to characterize the local microstructure, and furthermore that the local flow field is sufficiently characterized by the mean superficial velocity $\vec{U}$, and that Eq. 7 is valid down to the scale of single particle, then, we can calculate the drag on a single particle in a straightforward way via Eq. 10. The distribution of the difference

$$\Delta F_i^{LB,II} = \frac{F_{f,i}^{LB} - F_{f,i}^{II}}{\langle F_f^{LB} \rangle} \qquad (17)$$

of the "true" drag obtained from simulations and the one calculated from Eq. 10 is shown in Figure 8.

One sees that the maximum deviation is larger compared to results shown in Figure 4, hence, the agreement of DNS results and DP model prediction deteriorates. The fluctuations are not evenly distributed. For a larger fraction of the particles, the predicted force based on the local porosity is larger than the DNS result, leading to a negative $\Delta F_i^{LB,II}$.

Figure 9 shows the mean relative deviation s^{II}

$$s^{II} = \sqrt{\frac{\sum_{i=1}^{N_P} (\Delta F_i^{LB,II})^2}{N_P - 1}} \qquad (18)$$

for different porosities. As in Figure 5 an increase of the standard deviation with porosity is observed, however, the standard deviation is larger than in Figure 5.

Influence of distant particles on the individual fluid-particle force

From the previous sections, it is clear that a more accurate prediction of the fluid–particle force on individual particles, is only possible if the drag model takes into account some measure of the microstructure and the local flow field for each particle. However, the gas phase is described by the averaged Navier–Stokes equations and, thus, by construction

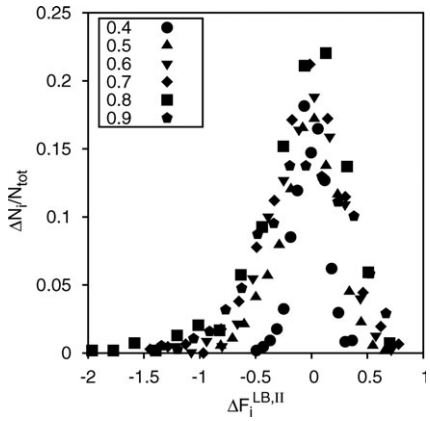

Figure 8. Deviation predicted drag force on individual particles using the local porosity from simulation results.

Note that the error in the force on individual particles due to grid resolution and other numerical parameters is typically about 3% or less.

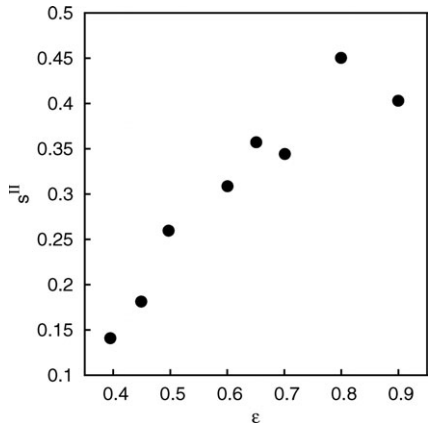

Figure 9. Standard deviation s^{II} of the difference of predicted drag force on individual particles using the local porosity from simulation results.

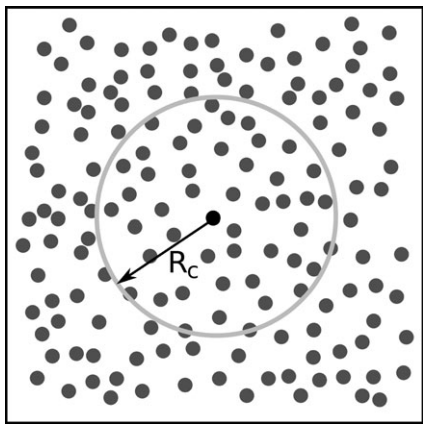

Figure 11. Schematic illustration of the creation of different random arrays with the microstructure fixed up to a certain distance from a marked particle.

All particles within the gray circle are kept at their current position, whereas the Monte–Carlo hard sphere algorithm is applied on the particles outside the circle to create new random arrays.

describes an averaged flow field and not the local flow field around each particle. If one wants a better prediction of the fluid–particle interaction on individual particles, one somehow has to reconstruct the ''local'' flow field from the average flow field, in combination with the detailed information on the particle phase, which seems impossible. This is demonstrated most clearly in Figure 10, which shows the flow field in a cross-section of the bed for a static configuration. The difference between the top and the bottom image is that only one particle is slightly displaced. It can be seen that the flow field is quite different, not only locally but also at a position away from the particle. Next, a quantification is given over what range fluctuations in the particle configuration will influence the flow field and hence the fluid–particle force. In other words, up to what distance do changes in the microstructure of a particle assembly influence the fluid–particle force on an individual particle, if the immediate surroundings are unchanged?

To this end, the size of the computational domain was fixed to be 10 times the particle diameter d_p. A configuration was created in the same way as described earlier. As shown in Figure 11, one test particle (with label $i = 1$) was selected and the whole configuration was shifted such that this particle was in the center of the domain. Subsequently, additional configurations were created from this initial one by changing only the positions of those particles which had a distance to the marked particle $|\vec{x}_i - \vec{x}_m|$ greater than a certain value R_c. Thus, in Figure 11, new configurations are created by displacing only those particles that are outside the circle with radius R_c. Unlike in the previous two sections, now, the direction of the velocity was the same for all simulations. The radii that we chose correspond to the minima of the radial distribution function of a hard sphere gas at a porosity of 0.5.

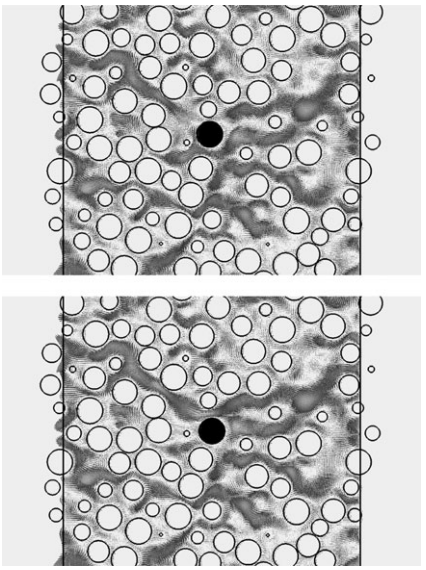

Figure 10. Slice through the 3-D array, showing the steady-state fluid flow field between the particles.

The difference between the top and bottom snapshot is that the black-solid particle is slightly displaced (20% of its diameter). Note that the particles are monodisperse; the apparent polydispersity is an effect of taking the cross-section.

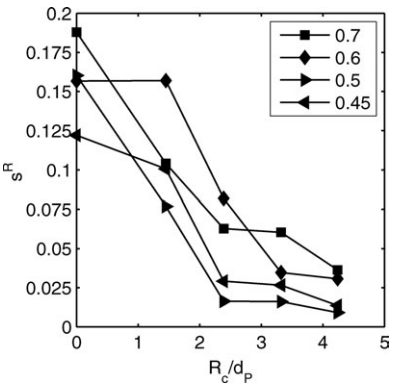

Figure 12. Standard deviation s^R (19) of the fluid–particle force on the test particle for different porosities as a function of the Radius R_c at which the structure of the assemblies was changed.

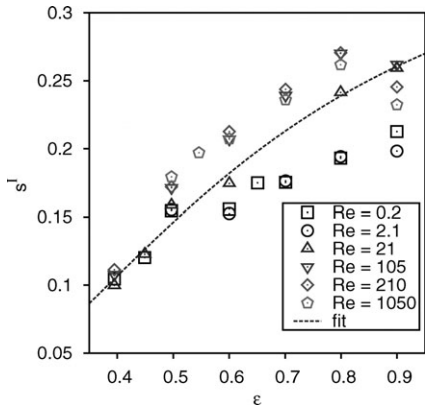

Figure 13. Standard deviation s^I as a function of the porosity for different Reynolds numbers *Re*.

The solid line represents a fit given by Eq. 21 for $Re = 21$.

Figure 12 shows the mean relative deviation s^R

$$s^R = \sqrt{\frac{\sum_{n=1}^{N_c}\left(\frac{F_{f,1}^{\mathrm{LB},n}-\langle F_{f,1}^{\mathrm{LB}}\rangle}{\langle F_{f,1}^{\mathrm{LB}}\rangle}\right)^2}{N_c-1}} \tag{19}$$

where $F_{f,1}^{LB,n}$ is the DNS fluid–solid force on the test particle 1 (projected on the direction of the flow) for a particular configuration n. Note that the average is now over the different configurations (N_c in total) and not over the particles in the domain. For $R_c = 0.0$, the standard deviation is, as expected, the same as in Figure 5. An increase of the distance R_c at which the microstructure of the particle arrays is changed, yields a lower-standard deviation and levels off at a distance of about two times the particle diameter d_P. This is clearly seen for the dense arrays with a porosity of $\varepsilon = 0.5$ and $\varepsilon = 0.45$, where it drops from about 0.1 to 0.03. For higher porosities, the standard deviation levels off at a higher value of about 0.1. The conclusion is that any type of closure for the drag on individual particles in DP model type simulations needs to take into account the microstructure of the particle assembly in the neighborhood of the particle up to at least rwo times its diameter.

Application of a modified drag model in DP simulations

To demonstrate to what extent the fluctuation of the force on individual particles might influence in macroscopic properties typically measured in fluidized bed experiments or simulations, we performed a DPM simulation of a small fluidized bed comprising of $N_P = 20{,}000$ particles.

The width W, depth D, and height H of the bed are chosen as $W \approx 55.8d_P$, $D \approx 5.6d_P$ and $H \approx 111.6d_P$. Note that a depth of $D = 5.6d_P$ ensures that the particles do not get stuck between front and back walls.[15] The physical properties of air are used for the density ρ_f and the dynamic viscosity η_f, whereas particle diameter d_P and particle density ρ_P are set to $d_P = 10^{-3}$m and $\rho_P = 1000$ kg/m^3, which in the Geldart classification corresponds to B-type particles. The superficial gas-velocity was set to be equal to approximately two times the minimum fluidization velocity. Particle–particle and particle-wall collisions are considered to be fully elastic and frictionless and free-slip boundary conditions were used on the sidewalls of the computational domain.

Thus far in this work, we have considered Stokes flow. However, for the fluidized bed we are considering, the Reynolds number will be larger than one, where the average Reynolds number is about 35. Therefore, we have repeated the analysis of Figures 4 and 5 also for higher Reynolds numbers, where for the average drag we used the correlation by Beetstra et. al.,[16] which is basically an extension of Eq. 7

$$F = \frac{10\,(1-\varepsilon)}{\varepsilon^3} + \varepsilon\left(1+1.5\sqrt{1-\varepsilon}\right) + \frac{0.413\mathrm{Re}}{24\varepsilon^3}\,\frac{\varepsilon^{-1}+3\varepsilon(1-\varepsilon)+8.4\mathrm{Re}^{-0.343}}{1+10^{3(1-\varepsilon)}\,\mathrm{Re}^{-(1+4(1-\varepsilon))/2}} \tag{20}$$

The result for the variance in the drag force for different Re numbers is shown in Figure 13. Although in principle, the force fluctuations depend on Re, for the current "proof-of-principle" simulation, we used the Re-independent fit

$$s^I_{\mathrm{fit}} = \frac{1}{\varepsilon^{-2.09}+2.59} \tag{21}$$

which is the dashed line in Figure 13.

We have compared the simulation results using two different drag models: (1) the standard drag F as calculated from Eq. 20, and (2) a fluctuating drag F_{fl} calculated from

$$F_{\mathrm{fl}} = (1+\sigma_F)F \tag{22}$$

where σ_F is a random number taken from a Gaussian distribution with zero mean and a standard deviation s^I + fit, taken from Eq. 21. We have added these random force at each time that the flow field is updated, that is, with a time interval of 10^{-5} s. During this interval, the configuration of the particles has changed appreciable. To test the effect of the time interval, we have also performed a simulation in which the fluctuating force was added every 10^{-6}, which is the timestep used for integrating the equation of motion of the particles. We did not found any significant differences compared to the simulations using a larger time interval.

In Figure 14, we show the average particle height

$$\langle r_z(t)\rangle = \frac{1}{N_P}\sum_{i=1}^{N_P} r_{z,i}(t) \tag{23}$$

and the RMS deviation of the particle velocity, in other words, the square root of the granular temperature

$$\underset{\mathrm{RMS}}{\Delta}\vec{v}(t) = \sqrt{\theta_T} = \sqrt{\frac{1}{3N_P}\sum_{n=1}^{N_P}[\vec{v}_n(t)\cdot\vec{v}_n(t)] - \langle\vec{v}(t)\rangle^2} \tag{24}$$

as a function of the time. As one would expect, we find that the granular temperature is higher in the results from the simulations with the fluctuating drag force (Eq. 22). As a consequence of the higher-relative movement of the particles, we also find that the bed expansion is larger in the simulations with the fluctuating drag. It is interesting to note that Goldschmidt et. al.[17] also found a larger bed expansion in their experimental results which they compared to DPM and TFM simulations, even though they studied slightly different systems.

Conclusions

In this article we have performed a study of the effect of local heterogeneities on the drag force, which is essentially

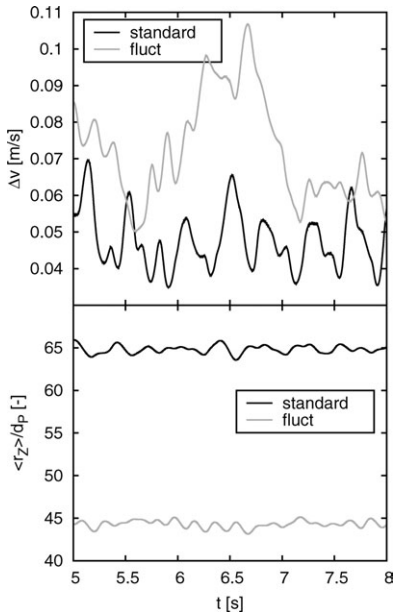

Figure 14. Mean *z*-Position and granular temperature of all particles as a functions of time: "standard" denotes the results of the simulation with the standard drag model (20) and "fluct" the results obtained with a modified drag model (22), which adds a random component to the drag force based on the results presented in the previous sections.

different from other studies in the literature on the effect heterogeneous structures and related approaches to account for this by filtering[18] or application of the energy-minimization multiscale method.[19] These latter methods assume that there is uniform drag force on the particles within a cell; it is only the magnitude of this average force which is modified due to the presence of heterogeneous structures. This still neglects the fact that when there are heterogeneous structures within a cell, two particles within the same cell may feel a very different drag force, which is the subject of our study.

In this article we have analyzed the fluctuations of the drag force on individual particles with respect to the mean drag in random static arrays of monodisperse particles. It was found that the drag on individual particles can differ considerably (up to 40%) from the mean. As the drag force calculated for individual particles in DP models is actually the mean drag in a random ensemble, this force thus differs substantially from the "true" drag force (that is, the drag force one would have in fully resolved simulations) even for systems which would be considered as homogeneous. Clearly for truly heterogeneous systems, the situation will become even worse.

As in DP model simulations, the particle positions are explicitly known, one might be tempted to use a local porosity to get a better prediction of the drag force. However, we found that by using a Voronoi tessellation-based local porosity the difference of DNS result and drag model on average increases. Compared to the deviations one finds using mean values of the porosity, a too large drag is calculated for a larger fraction of the particles and also the maximum difference is larger. This can qualitatively be understood by considering that a flowing fluid will minimize its resistance and thus less fluid will flow through regions with a locally lower porosity. As the effects of lower local porosity and lower local velocity are opposite to each other, using the local porosity without considering variations in the local velocity, a too high drag is calculated. Unfortunately, the variations in the local velocity are influenced not only by the nearest surroundings but also by changes in the microstructure at larger distances from the particle of which one seeks to calculate the drag. Although for dense systems (mean porosity of about 0.5 or lower), larger influence can only be seen for variations in the particle-phase microstructure at a distance of less than 2 particle diameters, for "dilute" systems ($\varepsilon \geq 0.6$), the root mean square deviation of the drag on an individual particle from its mean is about 10% even for changes in the microstructure at distances larger than four particle diameters. Our conclusion is therefore that it is unlikely that one can construct a deterministic closure which accurately (say within 5%) predicts the drag force on individual particles in DP models that is less expensive in terms of computational time than a fully resolved simulation. Rather one should consider the drag force as still being modeled on the length scale used to describe the fluid, in other words, on a TFM scale. Note that this study has been performed for homogeneous systems. For heterogeneous systems, the deviation of the actual drag and the one calculated from correlations like Eq. 9 will be much larger. That is, s^I should be regarded as the basic level of inaccuracy inherent to DP models. We nevertheless showed that the effect of the fluctuations in the drag force for a fluidized system are not negligible. It should be stressed that the purpose of these simulations is only to show that the fluctuations are big enough to have an impact, and we do not claim that the use of a drag with a fluctuating component added is necessarily an improvement over the existing drag correlations. The true test of the DPM will lie in a one-to-one comparison with a fully resolved fluidized bed simulation, which we will address in future studies.

Acknowledgments

The authors thank Anthony Ladd for useful discussions and suggestions and also for allowing us to use his lattice Boltzmann suspension code. This work is financially supported by the Netherlands Organisation for Scientific Research (NWO).

Literature Cited

1. Zhang D, Prosperetti A. Momentum and energy equations for disperse two-phase flows and their closures for dilute suspensions. *Int J Multiphase Flows*. 1997;23:425–453.
2. Drew D, Wallis G. *Fundamentals of two-phase flow modeling. Two-Phase Flow Fundamentals*, vol. 8 of *Multiphase science and technology*, Wallingford, CT: Begell House, 1994:1–67.
3. Jackson R. *The Dynamics of Fluidized Particles*. New York: Cambridge University Press, 2000.
4. van der Hoef M, van Sint Annaland M, Deen N, Kuipers J. Numerical simulation of dense gas-solid fluidized beds: a multiscale modeling strategy. *Ann Rev Fluid Mech*. 2008;40:47–70.
5. Kitagawa A, Murai Y, Yamamoto F. Two-way coupling of Eulerian-Lagrangian model for dispersed multiphase flows using filtering functions. *Int J Multiphase Flows*. 2001;27:2129–2153.
6. Ouyang L, Li J. Particle-motion-resolved discrete model for simulating gas-solid fluidization. *Chem Eng Sci*. 1999;54:2077–2083.
7. Helland EH, Ocelli R, Tadrist L. Numerical study of cluster formation in a gas-particle circulating fluidized bed. *Powder Technol*. 2000;110:210–221.
8. van Wachem B, van der Schaaf J, Schouten J, Krishna R, van den Bleek C. Experimental validation of Lagrangian-Eulerian simulations of fluidized beds. *Powder Technol*. 2001;116:155–165.

9. Kafui K, Thornton C, Adams M. Discrete particle-continuum fluid modelling of gas-solid fluidised beds. *Chem Eng Sci*. 2002;57: 2395–2410.
10. van der Hoef M, Beetstra R, Kuipers J. Lattice-Boltzmann simulations of low-Reynolds-number flow past monodispere and bidisperse arrays if spheres: results for the permeability and drag force. *J Fluid Mech*. 2005;528:233–254.
11. Ladd A. Numerical simulation of particulate suspensions via discretized Boltzmann equation. Part 1. theoretical foundation. *J Fluid Mech*. 1994;271:285–309.
12. Verberg R, Ladd A. Lattice-Boltzmann simulations of particle-fluid suspensions. *J Stat Phy*. 2001;104:1191–1251.
13. Luchnikov V, Medvedev N, Oger L, Troadec JP. Voronoi-Delaunay analysis of voids in systems of nonspherical particles. *Phys Rev E*. 1999;59:7205–7212.
14. Koch D, Sangani A. Particle pressure and marginal stabilty limits for a homogeneous monodisperse gas-fluidized bed: kinetic theory and numerical simulation. *J Fluid Mech*. 1999;400:229–263.
15. Hoomans B. Granular dynamics of gas-solid two-phase flows. Ph.D. thesis, Chemical Engineering, University of Twente, 2000.
16. Beetstra R, van der Hoef M, Kuipers J. Drag force of intermediate Reynolds number flow past mono- and bidisperse arrays of spheres. *AIChE J*. 2007;53:489–501.
17. Goldschmidt M, Beetstra R, Jam K. Hydrodynamic modelling of dense gas-fluidised beds: comparison and validation of 3D discrete particle and continuum models. *Powder Technol*. 2004; 142:23–47.
18. Igci Y, Andrews A,, Sundaresan S, Pannala S, O'Brien T. Filtered two-fluid models for fluidized gas-particle suspensions. *AIChE J*. 2008;54:1431–1448.
19. Wang W, Li J. Simulation of gas-solid two-phase flow by a multi-scale CFD approach—extension of the EMMS model to the sub-grid level. *Chem Eng Sci*. 2007;62:208–231.

Manuscript received Apr. 27, 2011, and revision received Mar. 15, 2012.